

Nanoscale

Accepted Manuscript



This is an *Accepted Manuscript*, which has been through the Royal Society of Chemistry peer review process and has been accepted for publication.

Accepted Manuscripts are published online shortly after acceptance, before technical editing, formatting and proof reading. Using this free service, authors can make their results available to the community, in citable form, before we publish the edited article. We will replace this *Accepted Manuscript* with the edited and formatted *Advance Article* as soon as it is available.

You can find more information about *Accepted Manuscripts* in the [Information for Authors](#).

Please note that technical editing may introduce minor changes to the text and/or graphics, which may alter content. The journal's standard [Terms & Conditions](#) and the [Ethical guidelines](#) still apply. In no event shall the Royal Society of Chemistry be held responsible for any errors or omissions in this *Accepted Manuscript* or any consequences arising from the use of any information it contains.

Electromechanical Coupling in Single-Layer MoS₂ Suspended-Channel Transistors and Resonators

Rui Yang¹, Arnob Islam¹, Philip X.-L. Feng^{1,*}

*¹Department of Electrical Engineering & Computer Science, Case School of Engineering
Case Western Reserve University, 10900 Euclid Avenue, Cleveland, OH 44106, USA*

We report on the analysis of electromechanical coupling effects in suspended doubly-clamped single-layer MoS₂ structures, and the designs of suspended-channel field-effect transistors (FETs) and vibrating-channel nanoelectromechanical resonators. In DC gating scenario, signal transduction processes including electrostatic actuation, deflection, straining on bandgap, mobility, carrier density and their intricate cross-interactions, have been analyzed considering strain-enhanced mobility (by up to 4 times), to determine the transfer characteristics. In AC gating scenario and resonant operations (using 100MHz and 1GHz devices as relevant targets), we demonstrate that the vibrating-channel MoS₂ devices can offer enhanced signals (than the zero-bandgap graphene counterparts), thanks to the resonant straining effects on electron transport of the semiconducting channel. We also show dependence of signal intensity and signal-to-background ratio (SBR) on device geometries and scaling effects, with SBR enhancement by a factor of ~8 for resonance signal, which provide guidelines toward designing future devices with desirable parameters.

*Corresponding Author. Email: philip.feng@case.edu

Resonant nanoelectromechanical systems (NEMS) have been demonstrating increasing capabilities and prospects for applications in fundamental physics metrologies, sensing and detection of physical quantities near the ultimate limits, and ultralow-power signal processing at radio and microwave frequencies, thanks to their miniaturized sizes and masses, high speeds, and exceptional responsivities and sensitivities.^{1,2,3} Investigations on the approaches of coupling electrical and mechanical properties in movable nanostructures are an important path toward such prospects; and these also benefits from the emerging materials with attractive new properties, and new techniques of making new nanostructures. Lately, atomic layer two-dimensional (2D) crystals have enabled new types of NEMS resonators with interesting attributes; graphene, in particular, has been extensively studied for 2D NEMS, for its ultralow mass, outstanding elastic properties and superior strain limit (strength).^{4,5,6,7,8,9,10,11} Only adding to the attractions of graphene as a semimetal, 2D semiconducting crystals, such as atomic layers isolated from transition metal dichalcogenides (TMDCs), also make robust NEMS resonators,^{12,13} creating possibilities for directly coupling mechanical motions into the carrier transport in 2D transistors with sizable bandgap, in ways that may be different than in the graphene counterparts with zero bandgap. Among the TMDCs, molybdenum disulfide (MoS_2) is particularly interesting for its thickness-dependent and strain-tunable band structure^{14,15} and mobility¹⁶, in addition to its ultrahigh strain limit, high elastic modulus and low weight.^{17,18}

MoS_2 field-effect transistors (FETs) have been extensively explored for different MoS_2 thicknesses, contact materials and device structures, with high $I_{\text{on}}/I_{\text{off}}$ ratio of more than 10^8 and mobility (μ) dependent on thickness.^{19, 20, 21, 22, 23, 24, 25, 26} Recently, electron mobility of $1020\text{cm}^2/(\text{V}\cdot\text{s})$ for monolayer and $34,000\text{cm}^2/(\text{V}\cdot\text{s})$ for 6 layer MoS_2 devices at low temperature have been demonstrated by encapsulating MoS_2 in hexagonal boron nitride (h-BN) and using

graphene as electrical contact.²⁷ Room temperature mobility in this type of devices is 40-120cm²/(V·s), showing the strong promise of MoS₂ as a material for 2D electronics. MoS₂ nanomechanical resonators have also been demonstrated, showing frequency up to 83MHz²⁸ and quality (*Q*) factor up to 710.¹² While optical transduction has been performed for these MoS₂ resonators with pre-patterned cavities,^{12,28,29,30} understanding the electromechanical coupling and signal transduction, and their dependence on various device parameters in such structures, are highly desired. Although electromechanical coupling effects via gate voltage have been studied in carbon nanotube (CNT)³¹ and graphene⁵ resonators, the electromechanical coupling that incorporates both the gating effect and straining effect on mobility remains elusive. Further, as a 2D semiconductor with unique electrical and mechanical properties, electromechanical coupling effects in MoS₂ could be different from that in 1D CNTs and 2D semimetal graphene. While the study of strain effect on mobility has been attempted in MoS₂ transistors,³² these devices are substrate-supported multilayer MoS₂, and the mobility is nearly constant or slightly decreasing with increasing bending. The effect of straining on device mobility for single-layer suspended MoS₂ FETs, and its effect on nanomechanical resonance has not been studied.

In this work, we demonstrate analysis and modeling of electromechanical coupling effects in suspended single-layer MoS₂, and designs of suspended-channel MoS₂ transistors and resonators. In DC scenario of the suspended MoS₂ FETs, we analyze the multi-physics effects on the channel conductance upon electrostatic gating, especially straining effect on enhancing mobility. We solve the electrostatic force and static deflection self-consistently, by first assuming no deflection, and calculate the electrostatic force, then calculate the amount of deflection that the force induces, which in turn increases the electrostatic force; we keep performing the calculation till the solutions of both the electrostatic force and the deflection converge. Moreover, we

include the mechanical pull-in effect in a modified configuration (with high- κ dielectric) and explore it as a way to improve $I_{\text{on}}/I_{\text{off}}$ ratio at low operating voltage. From the results obtained in the DC FET modeling, we perform AC and resonance analysis. We demonstrate that by considering the multi-physics coupling in both DC and AC situations, the signal-to-background ratio (SBR) exhibits significant enhancement of up to ~ 8 times, compared to previous analyses where only gating and capacitance change are considered. We further study the geometric effects on the DC and AC conductance, for varying channel length (L) and initial air gap (g_0), and we observe interesting scaling and dependency between device geometry and the SBR. The analyses provide important guidelines for future experiments toward efficient electrical readout of suspended single-layer MoS₂ vibrating-channel transistors (VCTs). This platform can also be extended to other 2D semiconductors such as WSe₂ and black phosphorus.

When we apply DC or AC gate voltage to the suspended MoS₂ device (Figure 1a), there will be several effects that modulates the channel conductivity (Figure 1b). In DC analysis, first, similar to substrate-supported MoS₂ FETs, the gate voltage (V_G) modulates the carrier density in the channel by changing the Fermi level of MoS₂. Second, V_G induces deflection in MoS₂ (shown by the blue arrow on the top right of Figure 1b), which changes the capacitance between MoS₂ and the back gate, and thus changes the carrier density. Note that there is an intricate problem that the electrostatic force induces displacement, which increases the capacitance, and further changes the electrostatic force. To solve this problem and obtain the displacement at certain V_G , we develop a Matlab program to calculate the solution of both electrostatic force and displacement self-consistently. Third, the displacement induces strain in the device, which reduces the bandgap of MoS₂,^{14,15} and thus shifts the threshold voltage (V_T). The shift in bandgap may also influence the carrier density, by altering the Fermi level;³³ but it has been

found theoretically that for monolayer MoS₂, Fermi level does not change much with the application of tensile strain,³⁴ thus we consider this effect to be small for monolayer devices. Finally, the strain changes the band structure, which changes the effective mass of electrons and reduces phonon scattering, thus enhancing the mobility^{35,36} (shown by the arrows on the right in Figure 1b). After the carrier density and mobility are determined, we can obtain the channel conductance and drain current (I_D) at varying gate voltage, and acquire the transfer characteristics (I_D - V_G curve) of the device (Figure 2). For AC and resonant operations with an added small AC gate voltage, we make use of the DC analysis results, and calculate the near-resonance characteristics while also considering multiple parameters such as the strain effect on mobility, which differs from previous analyses on graphene resonators (where several paths illustrated in Figure 1 are not considered).

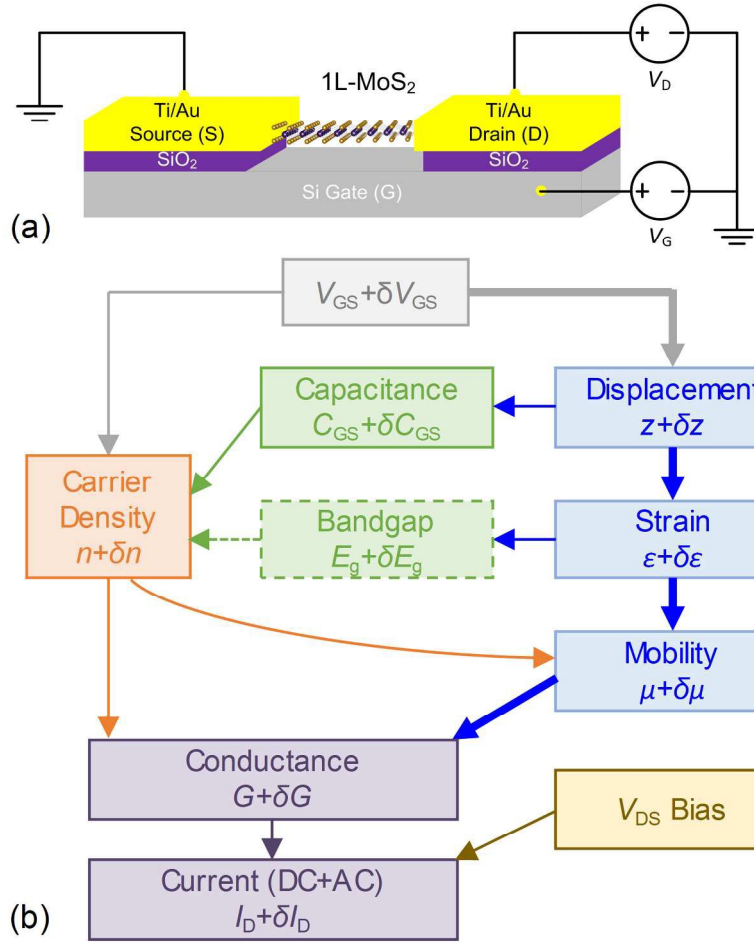


Figure 1. Illustrations of the suspended MoS₂ vibrating-channel transistor and its signal transduction diagram. (a) The schematic of the device with simplified DC electrical connection to the device. (b) Signal transduction diagram for the analysis of the device characteristics under applied DC and AC voltages and the effect on the measured current.

The DC analysis results for a suspended single-layer MoS₂ transistor with MoS₂ length $L=2\mu\text{m}$, width $w=1\mu\text{m}$, thickness $t=0.65\text{nm}$, and initial air gap $g_0=290\text{nm}$ are shown in Figure 2.

The static deflection (z_s) at certain V_G can be obtained by solving the following two equations:³⁷

$$-\frac{64}{3L^3}z_s^3 - \frac{8\varepsilon_0}{L}z_s + \frac{F_E L}{E_{Y,2D}} = 0 \quad (1)$$

$$F_E = \frac{1}{2} \frac{\epsilon_0'}{(g_0 - z_s)^2} V_g^2 \quad (2)$$

where ϵ_0 is the pre-strain (*i.e.*, initial strain), F_E is the electrostatic force on MoS₂ induced by the back gate, $E_{Y,2D}$ is the 2D Young's modulus (180N/m for monolayer MoS₂), ϵ_0' is vacuum permittivity. At the initial air gap, we can perform a calculation of F_E using equation 2, then we obtain the z_s due to the F_E by solving equation 1. With the new air gap $g=g_0-z_s$, we calculate F_E again, and get another z_s . We keep doing this iterative calculation till the fractional difference of both z_s and F_E between two calculation steps are smaller than 10^{-4} . With the z_s , we can calculate the total strain in the device using $\epsilon = \frac{8z_s^2}{3L^2} + \epsilon_0$,³⁷ and then obtain the mobility corresponding to the strain level using the relationship in Figure 2c inset.³⁵

With the deflection and mobility, we can calculate the transfer characteristics (I_D - V_G) of the vibrating-channel transistor using the 2D materials transistor model.³⁸ Using the displacement at certain gate voltage V_G , we determine the characteristic length using $\lambda = \sqrt{\frac{\epsilon_{MoS_2}' t (g_0 - z_s)}{\epsilon_0'}}$, where $\epsilon_{MoS_2}' = 4.5\epsilon_0'$ is the permittivity of MoS₂. We do not explicitly calculate the carrier density, because it later merges with the current calculation. We then calculate the current in two steps. First, with the drain voltage V_D applied, the source and drain electrostatic potentials (ϕ_S and ϕ_D) are obtained numerically using equation (6) in Reference [38]. Second, the current is obtained using equation (8) in Reference [38]. In the calculation, we assume MoS₂ is doped n-type with work function $\phi_{MoS_2} = 4.2\text{eV}$, and the flat-band voltage is $V_{FB} = 0.8\text{V}$ for back gate being p-type Si; impurity concentration $N_{imp} = 10^{13}\text{m}^{-2}$; 2D density of states $N_{DOS} = 10^{14}\text{eV}^{-1}\text{cm}^{-2}$; temperature is room temperature (300K). In this study, we focus on the suspended MoS₂ channel, and do not

include the contact resistance, but they can be added into the model easily when considering various specific devices with Ohmic contact, in future experiments.

For lower pre-strain levels, we calculate the transfer characteristics assuming different ε_0 of 0.06%, 0.17%, 0.28% (Figure 2a), corresponding to 0.1N/m, 0.3N/m and 0.5N/m pre-tension, respectively, because they are reported to be in the range of pre-tension in MoS₂ resonators after mechanical exfoliation.¹² We find that the transfer curves with 0% and 0.06% pre-strain are quite similar, and the curve with 0.17% pre-strain is only slightly higher, showing that for very low pre-strain, the gate-voltage-induced strain is quite significant compared to the pre-strain (Figure 2a); specifically, for 0% pre-strain, the total strain at $V_G=30V$ is $\varepsilon=0.33%$, and this value changes to 0.34% and 0.37% for 0.06% and 0.17% pre-strain, respectively (Figure 2b). At 0.28% pre-strain, I_D , strain, and mobility are all evidently higher than other curves (Figure 2a-c). We also calculate the result without considering the strain effect on enhancing mobility, but include the other effects in Figure 1b (blue dash dot line in Figure 2a-c). We find that I_D and μ are lower than when we take into account the strain effect on mobility, especially at large V_G . In Figure 2d-f, we further examine the effect of higher pre-strain levels on the transfer characteristics of the suspended MoS₂ transistor with the same geometry. We observe that I_D is much higher with higher pre-strain, especially when comparing 1% pre-strain with 0.5% pre-strain (Figure 2d). An interesting difference with the transfer characteristics with lower pre-strain is that for ε_0 higher than 1%, the I_D - V_G curve at “On” state is relatively linear (Figure 2d), instead of curving up at high V_G at lower pre-strain (Figure 2a). This is mainly because the gate voltage induced strain is much lower than the pre-strain, and the total strain remains almost constant (Figure 2e), thus mobility and I_D changes very little with V_G , while mostly changes with pre-strain level (Figure 2f). Further, because at higher pre-strain (>2%), the mobility almost

does not change with strain any more (Figure 2c inset), the transfer characteristics for 2%-10% pre-strain are quite similar.

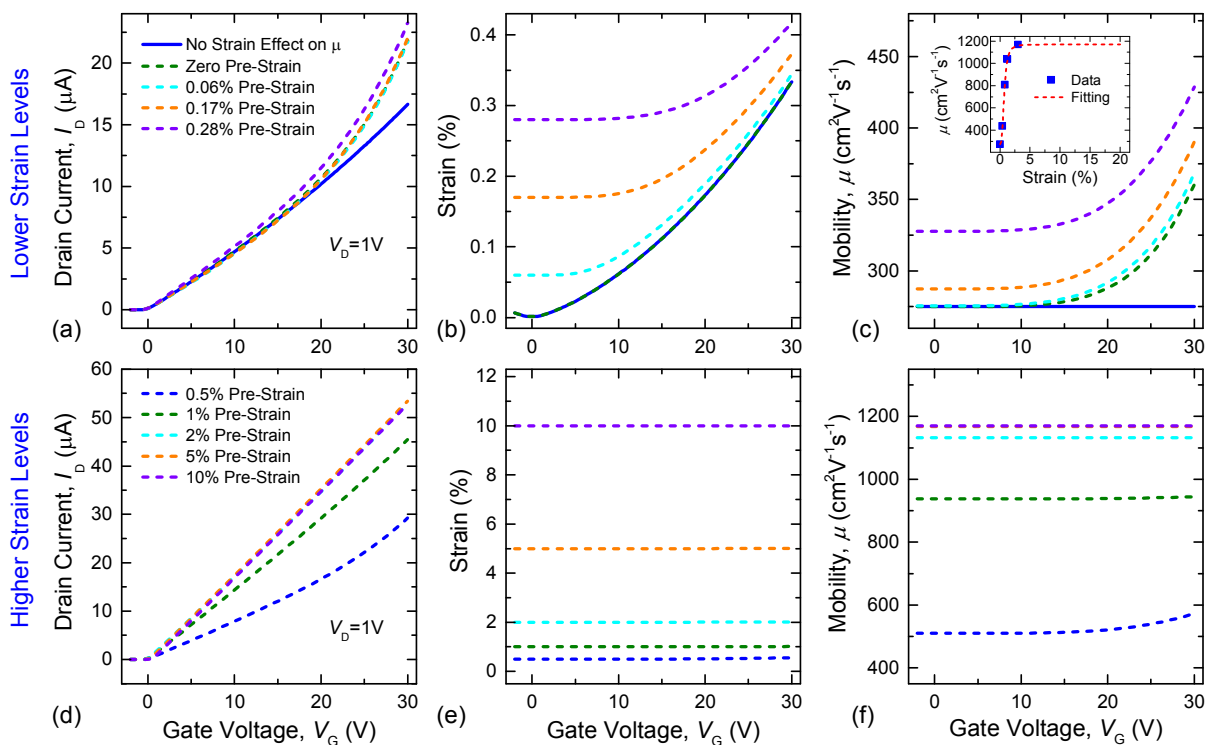


Figure 2. Calculated device performance when DC gate voltage is applied, for (a)-(c) lower, and (d)-(f) higher pre-strain level, for a suspended single-layer MoS₂ transistor with $L=2\mu\text{m}$, $w=1\mu\text{m}$, $g_0=290\text{nm}$. (a) Transfer characteristics (I_D - V_G) of the device under different pre-strain levels. (b) The total strain in the device with different V_G . (c) The electron mobility at different V_G . (d)-(f) has the same sequence as (a)-(c). Inset in (c) shows the extracted data points from theoretical calculation of mobility-strain relationship in reference [33], by assuming electron density n of $10^{11}/\text{cm}^2$.

For a field-effect transistor, I_D increases with decreasing L due to lower resistance. Besides, I_D of an air-gap coupled suspended FET also increases with decreasing g_0 due to higher capacitance. If we consider the strain effect on mobility, the trend will be different. We investigate I_D dependence on L and g_0 under two different conditions: lower pre-strain (0.2%) and higher pre-strain (5%) levels (Figure 3). At lower pre-strain level, although the maximum I_D

is obtained at the shortest L ($0.5\mu\text{m}$) and smallest g_0 (150nm), another sharp peak is observed at the longest L ($2\mu\text{m}$) and smallest g_0 (400nm) considered in our simulation (Figure 3a). The reason for this peak is that at longer L , larger deflection of the suspended channel is possible at the same V_G (15V) due to larger electrostatic force and weaker resistance to deflection. Higher deflection of channel results in larger strain, which induces higher mobility and increases I_D . On the contrary, for higher pre-strain level, deflection of the suspended channel at the same V_G is much smaller, and the strain will not increase much even for larger L . As a result, there is no peak at the longest L for higher pre-strain levels (Figure 3b). The observation is more obvious in Figure 3c, which shows the ratio between I_D with and without strain induced mobility enhancement ($I_{D,\text{Strain}}/I_D$), and the peak at the longest L and smallest g_0 for lower pre-strain level is observed. This ratio is almost constant for all L and g_0 for higher pre-strain level, achieving enhancement of I_D by a factor of ~ 4 after considering the strain effect. The subthreshold swing (SS) decreases with smaller air gap due to larger capacitance (Figure 3d); and at 30nm air gap, SS of 74mV/dec is expected.

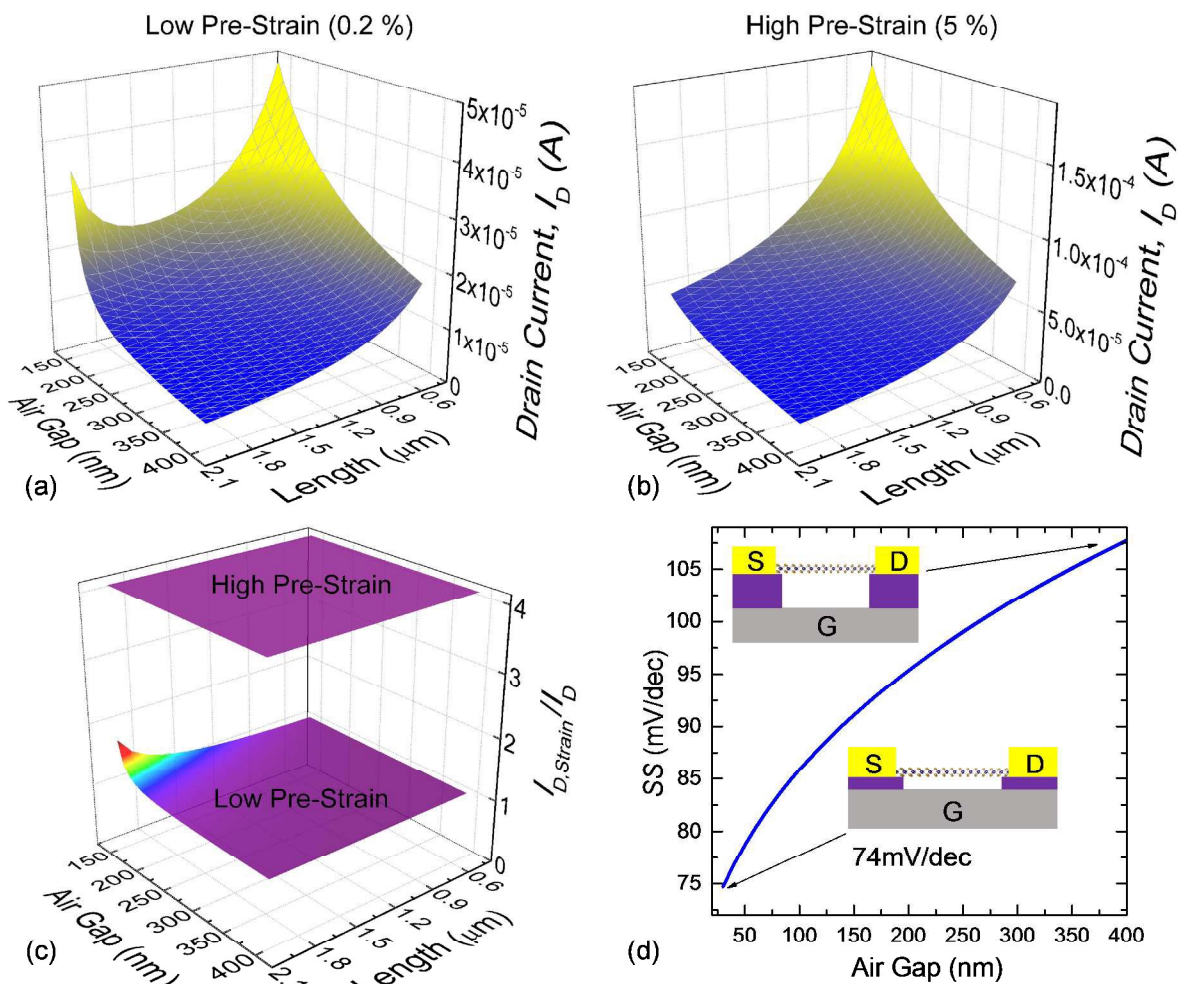


Figure 3. Dependence of drain current (I_D) on channel length (L) and air gap (g_0), computed for (a) low pre-strain and (b) high pre-strain levels, at $V_G=15V$ and $V_D=1V$. (c) The comparison of the ratio of drain current with and without strain induced mobility enhancement between low pre-strain and high pre-strain is shown. (d) The decrease of SS with the decrease of air gap.

We have simulated the effect of mechanical pull-in for this suspended single-layer MoS₂ FET due to the electrostatic force induced by V_G , using a slightly different geometry, by adding the 5nm to 10nm HfO₂ dielectric layer on silicon to prevent the gate from leaking after the mechanical pull-in, as illustrated in Figure 4a insets. For a suspended single-layer MoS₂ device, as we keep increasing V_G , the electrostatic force keeps increasing quadratically while the elastic

restoring force increases linearly with displacement, and beyond certain gate voltage called pull-in voltage (V_{PI}), the electrostatic force is always higher than the elastic force, and the MoS₂ channel is suddenly pulled down. At V_{PI} , there exists no solution to equations 1 and 2; and in the calculation, when the number of iterations reach 10000, we consider the pull-in effect occurs, and the suspended monolayer MoS₂ is suddenly pulled down. Figure 4a shows the mechanical pull-in at $V_{PI}=0.8V$ for a single-layer MoS₂ device with $L=5\mu m$, width $w=1\mu m$, and $g_0=60nm$, at 0.15% pre-strain. With the thin dielectric layer, the device is still functional as a normal FET after the pull-in happens. As a result of the abrupt pull-in, there is a sharp increase of drain current (Figure 4b). With shorter MoS₂ channel, V_{PI} increases from 0.65V ($L=9\mu m$) to 3.2V ($L=2\mu m$) for a device with $g_0=70nm$, and 0.2% pre-strain (Figure 4b). If we compare a regular, substrate-supported, non-suspended MoS₂ FET with 5nm HfO₂ (purple solid line in Figure 4c) to the suspended devices with pull-in effect, we can observe an improvement of the current on-off ratio from 3800 to 3.6×10^4 , if we take $V_G=-0.5V$ as off state and $V_G=3V$ as on state. V_{PI} increases with higher g_0 , from 1.2V at $g_0=70nm$ to 2.05V at $g_0=100nm$ (Figure 4c), and I_{on}/I_{off} ratio also increases with g_0 (Figure 4c inset). For logic circuit operation, it is desirable to define off state at $V_G=0V$, and this can be achieved by properly designing the geometry to maintain relatively high I_{on}/I_{off} ratio at the same time. Figure 4d shows that using $L=3\mu m$ device with g_0 varying from 60nm to 120nm, we achieve I_{on}/I_{off} ratio of 1.3×10^4 with 120nm air gap, when we take $V_G=0V$ as off state and $V_G=5V$ as on state. The I_{on}/I_{off} ratio also increases with increasing air gap, as shown in Figure 4d inset.

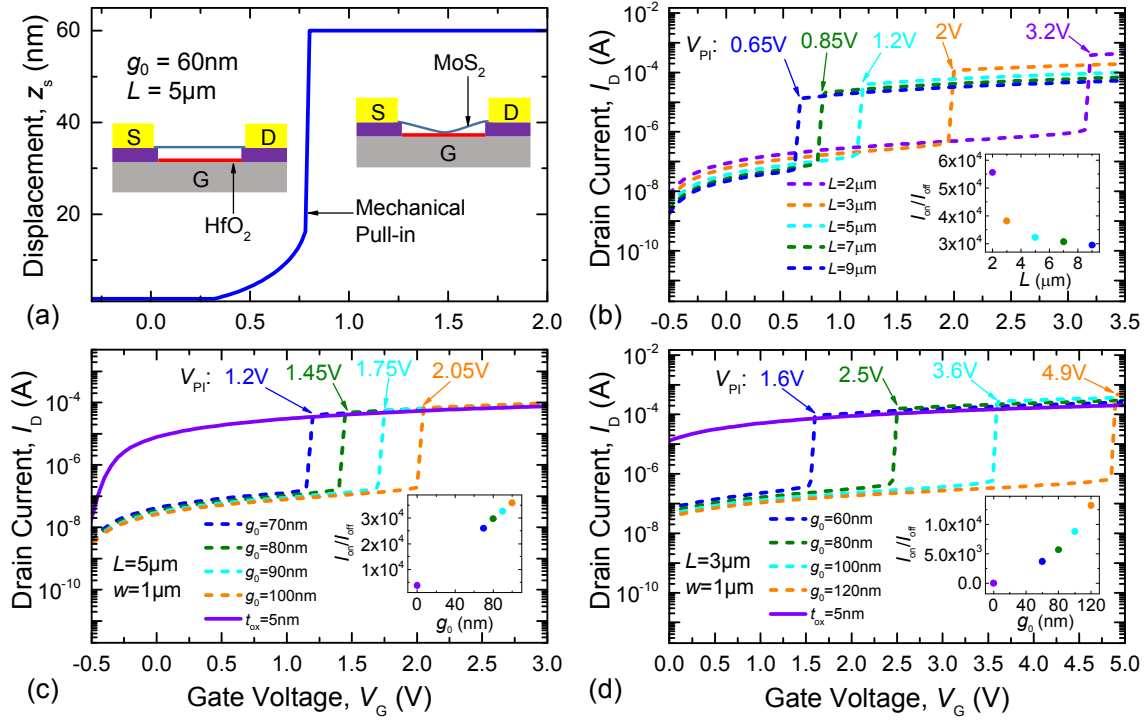


Figure 4. Investigation of mechanical pull-in effect on FET performance, with $V_D=0.1\text{V}$. (a) The displacement of the suspended MoS₂ FET at different V_G , showing the abrupt pull-in effect. Insets: Illustrations of the device structure before (left) and after (right) pull-in. (b) The effect of mechanical pull-in on suspended MoS₂ FETs with different L ($g_0=70\text{nm}$). Inset shows the change of current on-off ratio with L . (c) & (d) The comparison of mechanical pull-in effect on the suspended MoS₂ FET with different g_0 , for (c) $L=5\mu\text{m}$ and (d) $L=3\mu\text{m}$, at 0.2% pre-strain. Insets show the improvement of current on-off ratio with increasing air gap.

In AC operation near resonance, the response also increases after we take the strain effect into consideration (Figure 5a). For the monolayer MoS₂ resonator with $L=2\mu\text{m}$, $w=1\mu\text{m}$, and $g_0=290\text{nm}$, we calculate the device resonance at 100MHz assuming the device as a tensioned membrane (Figure 5b). The resonance frequency is expressed as $f_0 = \frac{1}{2L} \sqrt{\frac{\epsilon E_{Y2D}}{\rho \alpha}}$, where ρ is the 2D mass density and α is adsorbed mass coefficient. If we assume $\alpha=5$, then 1.4% pre-strain is necessary to achieve 100MHz resonance frequency, and the strain enhances the mobility and

changes the AC signal we can measure. The channel conductance with both DC and AC gate voltage is:

$$G(z) = G(z_s) + \frac{dG}{dV_G} \delta V_G + \frac{dG}{dz} \delta z, \quad (3)$$

$$\frac{dG}{dz} \delta z = \frac{dG}{dn} \frac{dn}{dz} \delta z + \frac{dG}{d\mu} \frac{d\mu}{dz} \delta z = V_G \frac{dG}{dV_G} \frac{C'_G}{C_G} \delta z + \frac{dG}{d\mu} \frac{d\mu}{d\varepsilon} \frac{d\varepsilon}{dz} \delta z, \quad (4)$$

where $G(z_s)$ is the conductance under static deflection (which only exists at DC and does not contribute to the signal at resonance frequency), C_G is the capacitance between the MoS₂ and the back gate, δV_G is the AC gate voltage where $\delta V_G = |\delta V_G| \cos(\omega t)$, δz is the AC deflection where

$$\delta z = |\delta z| \cos(\omega t + \varphi), \text{ with its amplitude } |\delta z| = \frac{C'_G V_G |\delta V_G|}{m \sqrt{(\omega_0^2 - \omega^2)^2 + (\omega_0 \omega / Q)^2}}$$

(m is the mass of the MoS₂ resonator), and $\varphi=0$ in ideal case. We can get dG/dV_G from the transfer characteristics under DC static deflection similar to that shown in Figure 2a,d, obtain $d\mu/d\varepsilon$ from the μ - ε relationship in

Figure 2c inset, and find $d\varepsilon/dz$ from the deflection relationship $\varepsilon = \frac{8z^2}{3L^2}$. The second term in

equation 4: $\frac{dG}{d\mu} \frac{d\mu}{dz} \delta z$ is a result of the strain effect in enhancing the mobility, which has not been

considered before for electromechanically transduced graphene resonator, but its effect is not negligible for suspended monolayer MoS₂ devices. Both the strain effect on mobility and the

mutual coupling effect between deflection and electrostatic force contribute to the enhancement

of dG/dV_G , which in turn increases the signal strength. As shown in Figure 5b, we find there is a

~4 times enhancement in the peak signal intensity and SBR for the 100MHz resonance. The

signal background is mainly determined by the $\frac{dG}{dV_G} \delta V_G$ term in equation (3). Here we assume

$V_G=15V$, $|\delta V_G|=1mV$ and $Q=1000$. Such Q should be achievable with high quality crystal and minimizing extrinsic damping effects, or measuring in higher vacuum or at low temperature, because Q of >700 has been achieved with fully-covered circular diaphragms measured in moderate vacuum (6mTorr),¹² and Q up to $\sim 10^4$ in doubly-clamped graphene resonators has been achieved at 5K.⁵ For 1GHz resonance in Figure 5c, we use $L=1\mu m$ and $\alpha=1$ to maintain pre-strain level lower than 10% to avoid metal-insulator transition in MoS_2 ,³⁹ and obtain that the ϵ_0 needed is 7.2%. With straining effect on mobility, the signal is much higher than without considering this effect. From Fig. 2c inset, the mobility does not increase much when pre-strain is higher than 5%, which means that $d\mu/d\epsilon$ term in equation (4) is very small, and thus $\frac{dG}{d\mu} \frac{d\mu}{d\epsilon} \frac{d\epsilon}{dz} \delta z$ is very small. Nonetheless, the current will still be enhanced at pre-strain level $\epsilon_0=7.2\%$, because the dG/dV_G term in equation (4) will be enhanced due to the much higher mobility induced by the strain. Note that the background level is also higher for 1GHz resonance, so the SBR is not much enhanced, which is different from the 100MHz device.

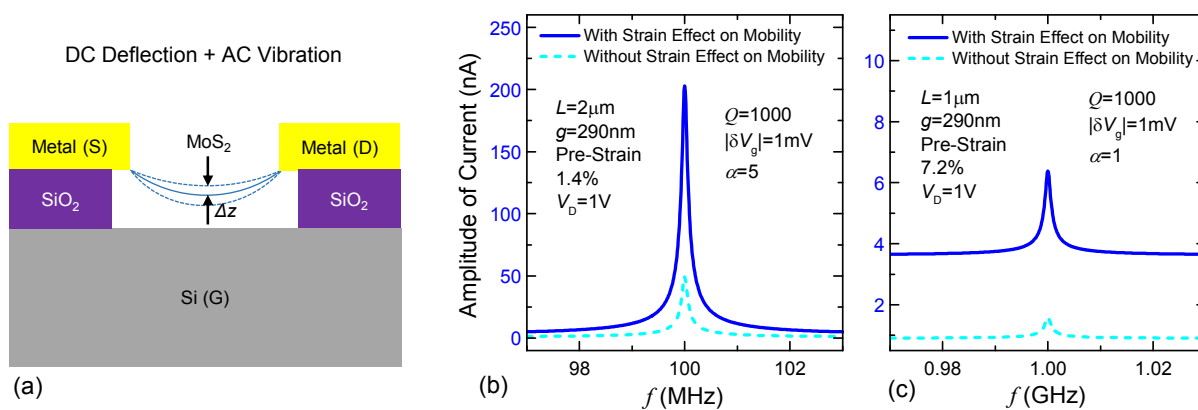


Figure 5. The calculated device performance when both DC and AC gate voltages are applied, showing the device resonance characteristics. The resonance considering the strain effect on mobility is compared with the resonance without considering that, for (a) 100MHz resonance, and (b) 1GHz resonance.

We further investigate the effect of varying the device dimension on the SBR, with comparison against the signal without considering the strain effect (Figure 6). For 100MHz case, we vary L from $0.5\mu\text{m}$ to $2\mu\text{m}$, and g_0 from 200nm to 400nm , and the SBR and SBR enhancement factor (ratio of SBR between considering and not considering the strain effect on mobility) are shown in Figure 6a,b. SBR as high as ~ 1435 has been projected, at $L=1.1\mu\text{m}$ and $g_0=200\text{nm}$ (Figure 6a). Smaller g_0 makes the electrostatic coupling more efficient, resulting in higher measured current. For length variation, we observe the interesting dependence, and at $L\approx 1.1\mu\text{m}$ we get the best SBR. The effect of L is intricate and it at least includes 4 aspects. Within the length range we consider, we use the effect of larger L as an example. First, with larger L , higher pre-strain is needed to attain the same resonance frequency, which translates into higher mobility and higher DC conductance; while the increasing L also results in higher resistance and lower conductance. The combination of these two effects makes dG/dV_G first decreases, and then increases with L . With larger dG/dV_G , the total $G(z)$ at resonance will be higher, and the background is also higher, which would result in lower SBR. Second, z_s increases with larger L , resulting in smaller g_s , higher capacitance, and especially, higher δz , which then increases both $G(z)$ and SBR. Third, larger L results in smaller $d\varepsilon/dz$, which decreases both $G(z)$ and SBR. Fourth, $d\mu/d\varepsilon$ also depends on the strain level, which again depends on L . With these different factors together influencing the total $G(z)$ and the background, we find that SBR depends on both L and g_0 (Figure 6a), while the SBR enhancement factor (ratio of SBR with and without considering the strain effect on mobility) mostly depends on L , with its highest value of 6.3 at $L=1\mu\text{m}$ (Figure 6b). The SBR clearly increases after we incorporate the strain effect on mobility. We also analyze the SBR and SBR enhancement factor for a 1GHz single-layer MoS₂ nanomechanical resonator (Figure 6c,d). We

consider same range of g_0 from 200nm to 400nm, while different range of L from 0.1 μm to 1 μm , compared to the 100MHz device, to keep the necessary strain relatively low. The peak SBR is ~ 23.8 when $L=2\mu\text{m}$ and $g_0=200\text{nm}$, which is smaller than 100MHz resonance, because the displacement is smaller at higher frequency (Figure 6c). We obtain highest SBR enhancement factor of ~ 8 at $L\approx 200\text{nm}$ and $g_0=200\text{nm}$, which is better than the 100MHz device. We also observe similar dependence on g_0 as the 100MHz device, with higher SBR enhancement factor at smaller g_0 (Figure 6d).

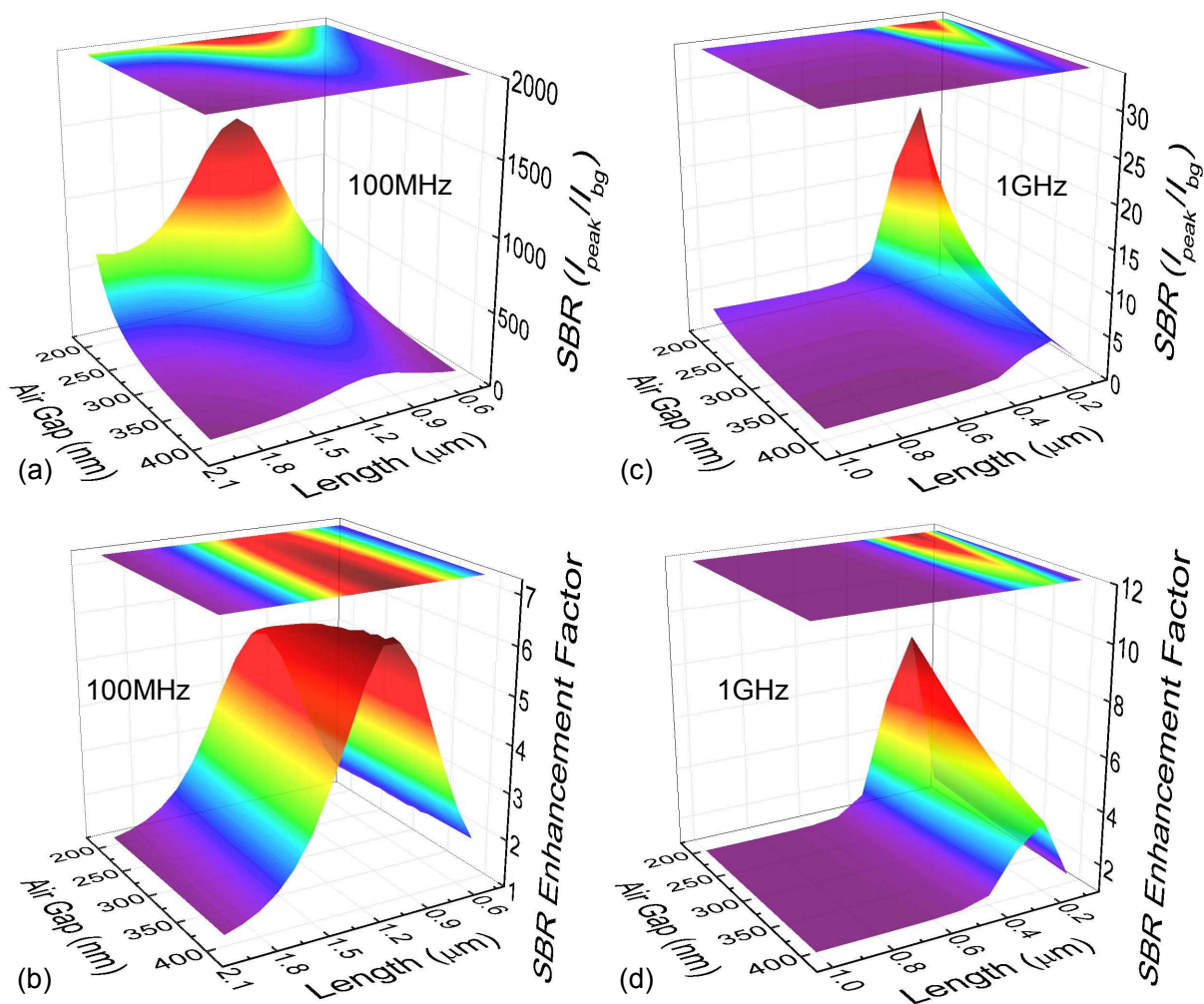


Figure 6. 3D color maps showing the effect of MoS₂ channel length and initial air gap on the resonance responses, with $V_G=15\text{V}$, $V_D=1\text{V}$, $|\delta V_G|=1\text{mV}$ and $Q=1000$. (a)-(b) 100MHz resonance for devices with

$L=0.5-2\mu\text{m}$, and $g_0=200-400\text{nm}$. (c)-(d) 1GHz resonance for device with $L=0.1-1\mu\text{m}$, and $g_0=200-400\text{nm}$. (a) & (c) The SBR of the resonances at (a) 100MHz, and (c) 1GHz, with the projection of the amplitude shown on the top. (b) & (d) The SBR enhancement factor, at (b) 100MHz, and (d) 1GHz.

Recently, piezoelectricity in single-layer MoS_2 has been experimentally verified,^{40,41} however, it should not have effect on the generic devices we consider here. First, the piezoelectric effect is only observed when the electrodes are configured along the zigzag direction, so that the bias electric field is along the armchair direction of the single-layer MoS_2 crystal.^{40,41} In this work, however, we consider generic MoS_2 suspended-channel FETs whose contact electrodes are in arbitrary orientations. Second, even if the drain-source electrodes happen to allow the bias electric field to be along the armchair direction, the occurrence of the piezoelectric effect relies on the Schottky barriers, and the strain-induced charge should asymmetrically modulate the Schottky barriers (the piezotronic effect).⁴⁰ In our calculations, however, we focus on the suspended MoS_2 channel rather than the contact electrodes, and we have assumed Ohmic contact without Schottky barriers, and the piezotronic effect will not be evident in this case, because the polarization and charge induced by piezoelectricity will not modulate the Schottky barriers and will be quickly neutralized by free carriers abundant in the electrodes and in MoS_2 channel. Third, for experimental realization of the device, Ohmic contact with small contact resistance has been achieved with graphene electrodes.²⁷ To rationally design devices to leverage the piezoelectricity effects, crystal orientation and Schottky barriers at the contacts should be carefully engineered, which is beyond the scope of this work.

In summary, we have analyzed the DC static and AC resonance responses of the suspended single layer MoS_2 VCT. Using the self-consistent calculation and taking the strain effect on mobility into consideration, we have first elucidated the effect on DC transfer characteristics, and

then extended the calculation to AC resonance analysis, showing that the signal will be higher after considering this effect. We have also examined the effect of geometry (*e.g.*, L and g_0) on DC and AC signal that can be measured, which provides important guidelines for future designs and experimental demonstrations of this type of devices.

Acknowledgement: We thank the support from Case School of Engineering, National Academy of Engineering (NAE) Grainger Foundation Frontier of Engineering (FOE) Award (FOE2013-005), National Science Foundation CAREER Award (Grant ECCS-1454570). We thank Z. Wang and J. Lee for helpful technical discussions.

References

- ¹ M. L. Roukes, *Phys. World*, 2001, **14**, 25-31.
- ² K. C. Schwab and M. L. Roukes, *Phys. Today*, 2005, **58**, 36-42.
- ³ A. N. Cleland, *Foundations of Nanomechanics: from Solid-State Theory to Device Applications*, Springer, New York, 2003, pp 303-340.
- ⁴ J. S. Bunch, A. M. van der Zande, S. S. Verbridge, I. W. Frank, D. M. Tanenbaum, J. M. Parpia, H. G. Craighead and P. L. McEuen, *Science*, 2007, **315**, 490-493.
- ⁵ C. Chen, S. Rosenblatt, K. I. Bolotin, W. Kalb, P. Kim, I. Kymissis, H. L. Stormer, T. F. Heinz and J. Hone, *Nat. Nanotechnol.*, 2009, **4**, 861-867.
- ⁶ A. M. van der Zande, R. A. Barton, J. S. Alden, C. S. Ruiz-Vargas, W. S. Whitney, P. H. Pham, J. Park, J. M. Parpia, H. G. Craighead and P. L. McEuen, *Nano Lett.*, 2010, **10**, 4869-4873.
- ⁷ A. Eichler, J. Moser, J. Chaste, M. Zdrojek, I. Wilson-Rae and A. Bachtold, *Nat. Nanotechnol.*, 2011, **6**, 339-342.
- ⁸ R. A. Barton, J. Parpia and H. G. Craighead, *J. Vac. Sci. Technol., B*, 2011, **29**, 050801.
- ⁹ C. Chen, S. Lee, V. V. Deshpande, G.-H. Lee, M. Lekas, K. Shepard and J. Hone, *Nat. Nanotechnol.*, 2013, **8**, 923-927.
- ¹⁰ V. Singh, S. Sengupta, H. S. Solanki, R. Dhall, A. Allain, S. Dhara, P. Pant and M. M. Deshmukh, *Nanotechnol.*, 2010, **21**, 165204.
- ¹¹ S. Lee, C. Chen, V. V. Deshpande, G.-H. Lee, I. Lee, M. Lekas, A. Gondarenko, Y.-J. Yu, K. Shepard, P. Kim and J. Hone, *Appl. Phys. Lett.*, 2013, **102**, 153101.
- ¹² J. Lee, Z. Wang, K. He, J. Shan and P. X.-L. Feng, *ACS Nano*, 2013, **7**, 6086-6091.
- ¹³ Z. Wang, J. Lee, K. He, J. Shan and P. X.-L. Feng, *Sci. Rep.*, 2014, **4**, 3919.
- ¹⁴ K. He, C. Poole, K. F. Mak and J. Shan, *Nano Lett.*, 2013, **13**, 2931-2936.
- ¹⁵ H. J. Conley, B. Wang, J. I. Ziegler, R. F. Haglund, S. T. Pantelides and K. I. Bolotin, *Nano Lett.*, 2013, **13**, 3626-3630.
- ¹⁶ R. Yang, Z. Wang and P. X.-L. Feng, *Nanoscale*, 2014, **6**, 12383-12390.
- ¹⁷ Q. H. Wang, K. Kalantar-Zadeh, A. Kis, J. N. Coleman and M. S. Strano, *Nat. Nanotechnol.*, 2012, **7**, 699-712.
- ¹⁸ R. Ganatra, and Q. Zhang, *ACS Nano*, 2014, **8**, 4074-4099.

- ¹⁹ B. Radisavljevic, A. Radenovic, J. Brivio, V. Giacometti and A. Kis, *Nat. Nanotechnol.*, 2011, **6**, 147-150.
- ²⁰ H. Liu, A. T. Neal and P. D. Ye, *ACS Nano*, 2012, **6**, 8563-8569.
- ²¹ S. Das, H.-Y. Chen, A. V. Penumatcha and J. Appenzeller, *Nano Lett.*, 2013, **13**, 100-105.
- ²² H. Nam, S. Wi, H. Rokni, M. Chen, G. Priessnitz, W. Lu and X. Liang, *ACS Nano*, 2013, **7**, 5870-5881.
- ²³ W. Bao, X. Cai, D. Kim, K. Sridhara and M. S. Fuhrer, *Appl. Phys. Lett.*, 2013, **102**, 042104.
- ²⁴ B. W. H. Baugher, H. O. H. Churchill, Y. Yang and P. Jarillo-Herrero, *Nano Lett.*, 2013, **13**, 4212-4216.
- ²⁵ H. Wang, L. Yu, Y.-H. Lee, Y. Shi, A. Hsu, M. L. Chin, L.-J. Li, M. Dubey, J. Kong and T. Palacios, *Nano Lett.*, 2012, **12**, 4674-4680.
- ²⁶ R. Yang, X. Zheng, Z. Wang, C. J. Miller and P. X.-L. Feng, *J. Vac. Sci. Technol., B*, 2014, **32**, 061203.
- ²⁷ X. Cui, G.-H. Lee, Y. D. Kim, G. Arefe, P. Y. Huang, C.-H. Lee, D. A. Chenet, X. Zhang, L. Wang, F. Ye, F. Pizzochero, B. S. Jessen, K. Watanabe, T. Taniguchi, D. A. Muller, T. Low, P. Kim and J. Hone, *Nat. Nanotechnol.*, 2015, **10**, 534-540.
- ²⁸ J. Lee, Z. Wang, K. He, J. Shan and P. X.-L. Feng, *Appl. Phys. Lett.*, 2014, **105**, 023104.
- ²⁹ A. Castellanos-Gomez, R. van Leeuwen, M. Buscema, H. S. van der Zant, G. A. Steele and W. J. Venstra, *Adv. Mater.*, 2013, **25**, 6719-6723.
- ³⁰ R. Yang, Z. Wang, P. Wang, R. Lujan, T. N. Ng and P. X.-L. Feng, In *Proceedings*, 28th IEEE International Conference on Micro Electro Mechanical Systems (MEMS 2015), IEEE, Estoril, Portugal, 2015, pp 877-880.
- ³¹ B. Lassagne, Y. Tarakanov, J. Kinaret, D. Garcia-Sanchez, and A. Bachtold, *Science*, 2009, **325**, 1107-1110.
- ³² H.-Y. Chang, S. Yang, J. Lee, L. Tao, W.-S. Hwang, D. Jena, N. Lu, and D. Akinwande, *ACS Nano*, 2013, **7**, 5446-5452.
- ³³ M.-Y. Tsai, A. Tarasov, Z. R. Hesabi, H. Taghinejad, P. M. Campbell, C. Joiner, A. Adibi and E. M. Vogel, *ACS Appl. Mater. Interfaces*, 2015, **7**, 12850-12855.
- ³⁴ P. Lu, X. Wu, W. Guo and X. C. Zeng, *Phys. Chem. Chem. Phys.*, 2012, **14**, 13035-13040.
- ³⁵ Y. Ge, W. Wan, W. Feng, D. Xiao and Y. Yao, *Phys. Rev. B*, 2014, **90**, 035414.

-
- ³⁶ S. Yu, H. D. Xiong, K. Eshun, H. Yuan and Q. Li, *Appl. Surf. Sci.*, 2015, **325**, 27-32.
- ³⁷ T. Low, Y. Jiang, M. Katsnelson and F. Guinea, *Nano Lett.*, 2012, **12**, 850-854.
- ³⁸ W. Cao, J. Kang, W. Liu and K. Banerjee, *IEEE Trans. Electron Devices*, 2014, **61**, 4282-4290.
- ³⁹ M. Ghorbani-Asl, S. Borini, A. Kuc and T. Heine, *Phys. Rev. B*, 2013, **87**, 235434.
- ⁴⁰ W. Wu, L. Wang, Y. Li, F. Zhang, L. Lin, S. Niu, D. Chenet, X. Zhang, Y. Hao, T. F. Heinz, J. Hone and Z. L. Wang, *Nature*, 2014, **514**, 470–474.
- ⁴¹ H. Zhu, Y. Wang, J. Xiao, M. Liu, S. Xiong, Z. J. Wong, Z. Ye, Y. Ye, X. Yin and X. Zhang, *Nat. Nanotechnol.*, 2014, 1–5.